PAPER

Genomic DNA-mediated formation of a porous $Cu_2(OH)PO_4/Co_3(PO_4)_2 \cdot 8H_2O$ rolling pin shape bifunctional electrocatalyst for water splitting reactions†

Harjinder Singh,‡[a] Imtiaz Ahmed, [iD] ‡[a] Rathindranath Biswas, [iD][a] Shouvik Mete,[a] Krishna Kamal Halder,[b] Biplab Banerjee[a] and Krishna Kanta Haldar [iD] *[a]

Among the accessible techniques, the production of hydrogen by electrocatalytic water oxidation is the most established process, which comprises oxygen evolution reaction (OER) and hydrogen evolution reaction (HER). Here, we synthesized a genomic DNA-guided porous $Cu_2(OH)PO_4/Co_3(PO_4)_2 \cdot 8H_2O$ rolling pin shape composite structure in one pot. The nucleation and development of the porous rolling pin shape $Cu_2(OH)PO_4/Co_3(PO_4)_2 \cdot 8H_2O$ composite was controlled and stabilized by the DNA biomolecules. This porous rolling pin shape composite was explored towards electrocatalytic water oxidation for both OER and HER as a bi-functional catalyst. The as-prepared catalyst exhibited a very high OER and HER activity compared to its various counterparts in the absence of an external binder (such as Nafion). The synergistic effects between Cu and Co metals together with the porous structure of the composite greatly helped in enhancing the catalytic activity. These outcomes undoubtedly demonstrated the beneficial utilization of the genomic DNA-stabilised porous electrocatalyst for OER and HER, which has never been observed.

Introduction

The architecture of productive catalysts to expedite the kinetics of electrochemical water oxidation is a key factor in the renewable energy conversation innovations. Researchers have prepared and amended different techniques to fabricate excellent catalysts, such as 2D NiCoFe,[1] cobalt phosphates $(Co_3(PO_4)_2)$,[2] $(Co_5(PO_4)_2(OH)_4)$,[3] Fe_2O_3,[4] $CuCo_2S_4/g-C_3N_4$,[5] $Co_2-P@FePO_4$,[6] Au/ZnO,[7] Au/Cu,[8] Co_2P/Co_2N,[9] and $DNA@Mn_3(PO_4)_2$.[10] Among them, porous nanostructured materials, with high porosity, have exhibited impressive properties in several applications, for example catalysis,[6,11–14] separation,[6,15] energy storage materials,[16–18] sensors,[19–21] and drug delivery.[22–24] Numerous synthesis methods, such as hydrothermal,[1] polymerization,[6] co-precipitation,[25,26] electrodeposition,[27,28] and

direct calcination methods,[2] were utilized to prepare porous nanostructured materials. Among all strategies, the soft-templating approach followed by calcination at high temperature is widely used for its benefits and minimal expense. However, this technique includes multiple steps to introduce reactant species into porous structures. In the soft-templating method the requirements for the alleviation of stringent amphiphilicity between the templating molecules and precursors as well as direct control over self-assembled structures possess a big challenge for its application.

To address these issues, the DNA molecular self-assemble approach was proposed as an alternative. The interactions of DNA molecules with different metal ions showed prolonged higher stability when the conditions were optimized properly. DNA can form a perfect metal-DNA self-assembly with both cationic and anionic species because of double-helical structure of DNA having A–T and G–C pairs, sugar moieties and phosphate groups. The metal-DNA self-assembly could exhibit varied catalytic activities based on the metal content, aspect ratio of metal DNA self-assemblies and the surface morphology of the material.

Although, various DNA-guided nanostructure materials are well-reported in literature,[9,10,29–37] to the best of our knowledge, a genomic DNA scaffold -driven porous $Cu_2(OH)PO_4/Co_3(PO_4)_2 \cdot 8H_2O$ rolling pin shape composite structure was not explored till date. Here, we fabricated the $Cu_2(OH)PO_4/$

[a]*Department of Chemistry, Central University of Punjab, 151001-Bathinda, Punjab, India. E-mail: krishankant.haldar@cup.edu.in*

[b]*Physics Department, Kirori Mal College, University of Delhi, Delhi, 110007, India*

† Electronic supplementary information (ESI) available: Additional data, such as instrumentation, detailed synthesis methods, details of fabrication of the working electrode, cyclic voltammograms (CV) and the corresponding electrochemical double layer capacitance, summary of electrochemical (Tables S3 and 4) powder XRD of $Cu_2(OH)PO_4$ and $Co_3(PO_4)_2 \cdot 8H_2O$ (Fig. S2), XRD Rietveld value (Tables S1 and 2) SEM images of $Cu_2(OH)PO_4/Co_3(PO_4)_2 \cdot 8H_2O$ in absence of DNA, Complete DNA sequence, BET study (Fig. S6) and TEM images of post catalytic are available in the ESI. See DOI: 10.1039/d1ra09098d

‡ H. S. and I. A. contributed equally to this work.

$Co_3(PO_4)_2 \cdot 8H_2O$ electrocatalyst for OER (in an alkaline solution) and HER (in an acidic solution) applications using genomic DNA, which can facilitate the formation and development of the porous $Cu_2(OH)PO_4/Co_3(PO_4)_2 \cdot 8H_2O$ rolling pin shape composite structure during drying at 50 °C. The structure and morphology of the as-synthesized $Cu_2(OH)PO_4/Co_3(PO_4)_2 \cdot 8H_2O$ composite were confirmed *via* different advance techniques. Further, this porous $Cu_2(OH)PO_4/Co_3(PO_4)_2 \cdot 8H_2O$ rolling pin shape composite structure exhibited an outstanding electrochemical OER and HER performance and high durability compared to its constituents. The electrochemical experimental results exhibited a superior OER performance with a small overpotential of 234 mV with a Tafel slope of 62 mV dec^{-1} at 10 mA cm^{-2}, and for HER it possessed a low overpotential of 138 mV with a Tafel slope of 41 mV dec^{-1} obtained at 10 mA cm^{-2} current density.

Result and discussion

The genomic DNA of the *Acorus Calamus* plant was used, and it also acted as the active binder between the catalyst and electrode. It is also well documented that DNA can control the morphologies of the nanostructured materials during their development process and these impacts are synergistic or competing, subject to the combination of the DNA sequence.[38] Thus, inspired by the versatility of DNA and its efficiency in guiding the nanostructure formation, we have prepared a genomic DNA-stabilized porous $Cu_2(OH)PO_4/Co_3(PO_4)_2 \cdot 8H_2O$ rolling pin shape composite structure in one pot. Extraction of DNA from the *Acorus Calamus* plant was done by following the Doley protocol, and the detailed extraction procedure[39,40] and synthesis of the porous $Cu_2(OH)PO_4/Co_3(PO_4)_2 \cdot 8H_2O$ structure were given in the ESI.† The one-pot $Cu_2(OH)PO_4/Co_3(PO_4)_2 \cdot 8H_2O$ porous composite synthesis was performed in the presence and absence of DNA to separately determine the impact of the DNA and formation of a porous rolling pin shape on the structural and electrocatalytic properties of the $Cu_2(OH)PO_4$ or $Co_3(PO_4)_2 \cdot 8H_2O$ components. Generated DNA sequences were deposited in the National Center for Biotechnology Information (NCBI)-GenBank (accession numbers: MZ713392), and the DNA nucleotide sequence was also given in the ESI.†

To investigate the phase composition of the as-synthesized DNA scaffold-driven porous $Cu_2(OH)PO_4/Co_3(PO_4)_2 \cdot 8H_2O$ rolling pin shape composite structure, X-ray diffraction (XRD) analyses were performed. As shown in Fig. 1, all the attributed indexed Bragg peaks have strongly supported the formation of the binary phase. However, all the well-matched peaks and the indexed peak at $2\theta = 15.23°$ (110 plane, d-spacing value 5.81 Å) helped to identify the presence of the orthorhombic copper phosphate hydroxide phase (#ICSD-200422). Simultaneously, the rest of the diffraction peaks (some were common) and particularly at 13.27° (020) provided the information of the hydrated monoclinic cobalt phosphate phase (#ICSD-065687). Also, the qualitative analysis of the phase fraction of the as-prepared sample was investigated by using the GSAS-II software. The phase fraction values of $Cu_2(OH)PO_4$ and

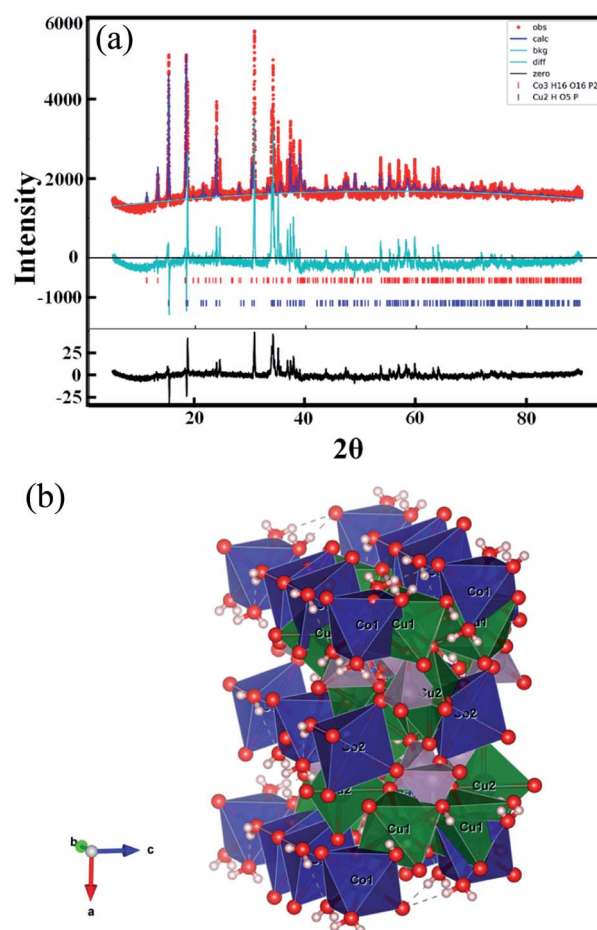**Fig. 1** (a) Rietveld refinement of the powder XRD pattern of $Cu_2(OH)PO_4/Co_3(PO_4)_2 \cdot 8H_2O$ with the reference patterns ICSD-200422 and ICSD-065687, (b) qualitative analysis of the crystal structure of $Cu_2(OH)PO_4/Co_3(PO_4)_2 \cdot 8H_2O$ using VESTA.

$Co_3(PO_4)_2 \cdot 8H_2O$ phases were found to be 0.61787 and 0.38213, respectively.

The new lattice parameter values after the Rietveld refinement (Tables S1, S2† and Fig. 1) were pretty close to the reference patterns, and established the presence of a binary phase in the $Cu_2(OH)PO_4/Co_3(PO_4)_2 \cdot 8H_2O$ rolling pin shape composite structure.

To gain more insights into the morphological and porosity investigation, scanning electron microscopy (SEM) and transmission electron microscopy (TEM) were explored. The FE-SEM image (Fig. 2a) clearly demonstrate the uniform morphology of the $Cu_2(OH)PO_4/Co_3(PO_4)_2 \cdot 8H_2O$ rolling pin shape composite structure. However, Fig. 2c shows the formation of a porous surface with the uniform shape of the $Cu_2(OH)PO_4/Co_3(PO_4)_2 \cdot 8H_2O$ rolling pin having the average size of 13 ± 0.2 μm in length and 2.82 ± 0.15 μm in width (Fig. 2b). The FE-SEM image (Fig. 2d) also reveals that nanorod bundles with small nanorods extruding from the two ends of the $Cu_2(OH)PO_4/Co_3(PO_4)_2 \cdot 8H_2O$ rolling pin. The elemental mapping analysis shows that the fundamental elements of the $Cu_2(OH)PO_4/Co_3(PO_4)_2 \cdot 8H_2O$ rolling pin were Cu, Co, P, O, N, and C, well-dispersed
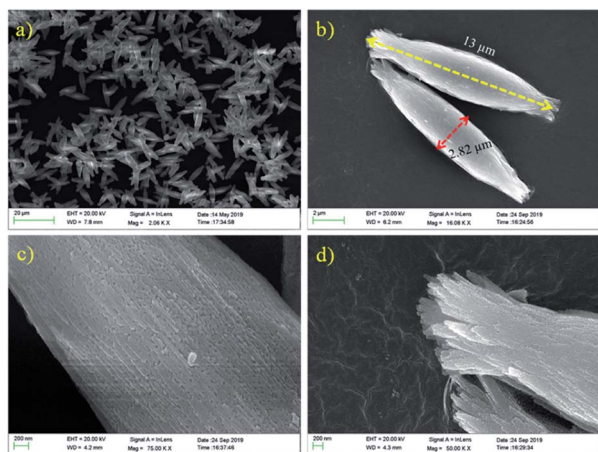
Fig. 2 (a and b) Low magnification FE-SEM image, (c and d) high magnification FE-SEM images of the $Cu_2(OH)PO_4/Co_3(PO_4)_2\cdot 8H_2O$ composites.

throughout the composite structure (Fig. S3†). However, no rolling pin shape of $Cu_2(OH)PO_4/Co_3(PO_4)_2\cdot 8H_2O$ was obtained in the absence of DNA under identical reaction conditions (Fig. S4†). TEM and HRTEM (Fig. 3a–c) analysis further supported the SEM investigation and confirmed the porous rolling pin structure of the $Cu_2(OH)PO_4/Co_3(PO_4)_2\cdot 8H_2O$ composite. The HR-TEM image exhibited that the nano-rolling pins are highly porous in nature (Fig. 3b).

Again, elemental composition and surface chemical state or valence states of $Cu_2(OH)PO_4/Co_3(PO_4)_2\cdot 8H_2O$ were studied *via* X-ray photoelectron spectroscopy (XPS), as presented in Fig. 4. The core peak of Cu 2p uncovers two main spin–orbit splitting at around 935.51 eV and 954.22 eV, corresponding to Cu $2p_{3/2}$ and Cu $2p_{1/2}$, which certified the presence of Cu^{2+} in the composite (Fig. 4a).[41] The two peaks located at 942.98 and 962.20 eV are the "shake up" satellites of Cu 2p. The Co 2p XPS exhibited two sharp peaks at binding energies of 780.9 eV ($2p_{3/2}$) and 796.6 eV ($2p_{1/2}$), which can be ascribed to the characteristic peak of Co^{3+}, and the two main peak located at 782.85 and 797.9 eV with two satellites peaks located at 786.2 and 802.3 eV confirmed the presence of Co^{2+}/Co^{3+} cations in $Cu_2(OH)PO_4/Co_3(PO_4)_2\cdot 8H_2O$ (Fig. 4b).[3,42–46] The P 2p area showed a single binding energy peak at 132.55, which was assigned to the P–O bonding presence in the composite (Fig. 4c).[43] O 1s signals are centred at 530.78 eV and 532.05 eV, which are assigned to the O1s core levels in the presence of phosphate species and water
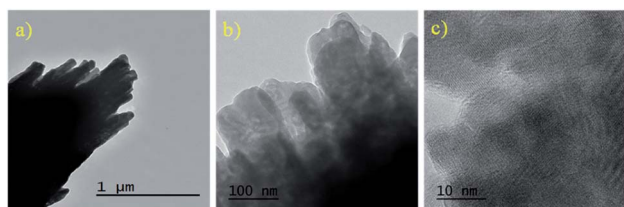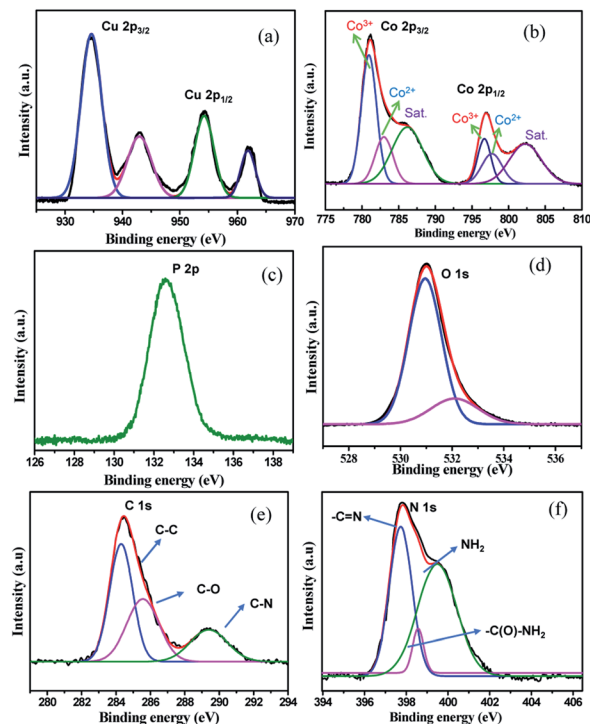

Fig. 4 XPS patterns of the $Cu_2(OH)PO_4/Co_3(PO_4)_2\cdot 8H_2O$ composite nanostructure: (a) Cu 2p, (b) Co 2p, (c) P 2p (d) O 1s and (e and f) C 1s, N 1s XPS spectra of DNA molecules, respectively.

molecules in $Cu_2(OH)PO_4/Co_3(PO_4)_2\cdot 8H_2O$, as presented in Fig. 4d. The C 1s high-resolution region (Fig. 4e) for the DNA-aided composite exhibits three distinct spin–orbit coupling originated peaks for different functional groups present in DNA molecules. Binding energy of the C–C bond appeared at 284.2 eV, for C–O bond at 285.6 eV and for C–N bond at 289.3 eV. Correspondingly, the deconvoluted XPS spectra of the N 1s orbital (Fig. 4f) showed the presence of distinct three spin–orbit coupling peaks, which originated at the binding energies of 397.8, 398.6, and 399.5 eV correlated with the –C=N, –NH_2, and –C(O)–NH_2 groups present in DNA, respectively. The existence of all component peaks with particular functional groups in the XPS spectra affirmed the presence of DNA, which mediated the formation of the $Cu_2(OH)PO_4/Co_3(PO_4)_2\cdot 8H_2O$ porous composite rolling pin.

Subsequently, to obtain proper information about the successful formation of the porous $Cu_2(OH)PO_4/Co_3(PO_4)_2\cdot 8H_2O$ composite rolling pin, which was exposed to the electrocatalytic OER performance by utilizing 1 M KOH solution as an electrolyte. Electrocatalytic tests for OER were employed *via* linear sweep voltammetry (LSV), cyclic voltammetry (CV) and electrochemical impedance spectroscopy (EIS) experiments. LSV curves were obtained at a scan rate of 10 mV s^{-1} in 1 M KOH (Fig. 5a). It was observed that pure $Co_3(PO_4)_2\cdot 8H_2O$, $Cu_2(OH)PO_4$ and IrO_2 exhibited relatively high overpotentials of 295 mV, 531 mV and 354 mV to obtain 10 mA cm^{-2} current density, respectively (Fig. 5a). Again, $Cu_2(OH)PO_4/Co_3(PO_4)_2\cdot 8H_2O$/DNA and $Cu_2(OH)PO_4/Co_3(PO_4)_2\cdot 8H_2O$ with an external binder

Fig. 3 (a and b) TEM images and (c) HR-TEM image of the $Cu_2(OH)PO_4/Co_3(PO_4)_2\cdot 8H_2O$ composite showing porosity.
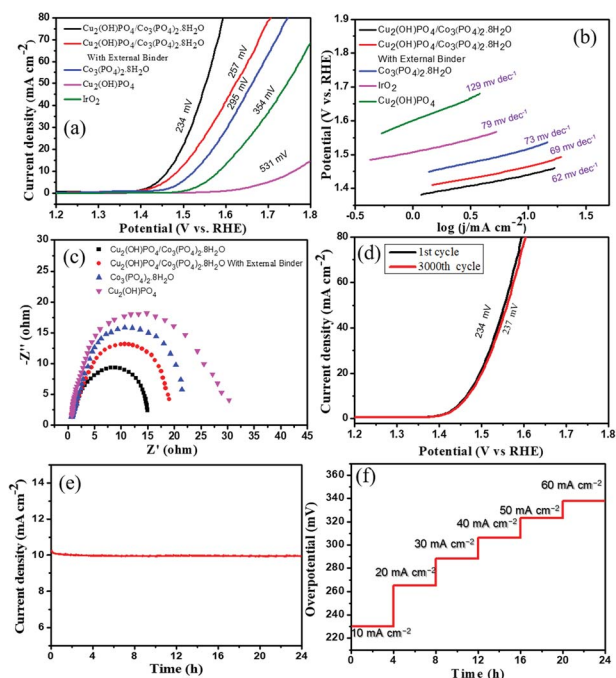
Fig. 5 (a) Linear sweep voltammograms plot, (b) the corresponding Tafel plot and (c) electrochemical impedance spectra (at 400 mV *vs.* Ag/AgCl) of $Cu_2(OH)PO_4/Co_3(PO_4)_2\cdot 8H_2O$, $Cu_2(OH)PO_4/Co_3(PO_4)_2\cdot 8H_2O$ with an external binder, $Co_3(PO_4)_2\cdot 8H_2O$, $Cu_2(OH)PO_4$ and IrO_2, (d) polarization curves of the $Cu_2(OH)PO_4/Co_3(PO_4)_2\cdot 8H_2O$ composite of 1st and 3000th cycles of continuous operation, (e) chronoamperometry study of the $Cu_2(OH)PO_4/Co_3(PO_4)_2\cdot 8H_2O$ composite catalyst at an overpotential of 234 mV for 24 h. (f) Chronopotentiometric study of $Cu_2(OH)PO_4/Co_3(PO_4)_2\cdot 8H_2O$ for OER in 1.0 M KOH as a function of the current density.

(Nafion) acquired overpotentials of 234 mV and 257 mV, respectively. This showed the prevalent strength and durability of the genomic DNA-stabilised $Cu_2(OH)PO_4/Co_3(PO_4)_2\cdot 8H_2O$ porous composite rolling pin interface devoid of the external binder, which was a profoundly important and commendable catalyst for OER under such highly alkaline conditions for reasonable applications. Further, to check out the kinetics of the OER progress, Tafel slopes were obtained from LSV curves, as shown in Fig. 5b. The $Cu_2(OH)PO_4/Co_3(PO_4)_2\cdot 8H_2O$ composite and $Cu_2(OH)PO_4/Co_3(PO_4)_2\cdot 8H_2O$ composite with an external binder catalyst showed low Tafel slope values of 62 mV dec^{-1} and 69 mV dec^{-1}, respectively. However, Tafel slopes for $Co_3(PO_4)_2\cdot 8H_2O$, $Cu_2(OH)PO_4$ and commercial IrO_2 were found to be 73 mV dec^{-1}, 129 mV dec^{-1}, and 79 mV dec^{-1}, respectively. This result clearly demonstrates that the genomic DNA-stabilised $Cu_2(OH)PO_4/Co_3(PO_4)_2\cdot 8H_2O$ porous composite rolling pin structure showed a superior OER activity over their counterparts. Electrochemical impedance spectroscopy (EIS) (Fig. 5c) analysis was carried out for all catalyst to estimate their charge transfer resistance. This result proved that the composites had better electrical conductivity, and the short electron transfer pathway suggested an easy electron transport during the OER process. Remarkably, the $Cu_2(OH)PO_4/Co_3(PO_4)_2\cdot 8H_2O$ catalyst displayed a smaller charge-transfer

resistance (R_{ct}) of 11.22 Ω than those of the other counterparts $Cu_2(OH)PO_4/Co_3(PO_4)_2\cdot 8H_2O$ with an external binder (12.96 Ω), $Co_3(PO_4)_2\cdot 8H_2O$ (16.43 Ω) and $Cu_2(OH)PO_4$ (22.84 Ω). The fast charge transfer process occurred in the interface between the catalyst surface and electrolyte for the $Cu_2(OH)PO_4/Co_3(PO_4)_2\cdot 8H_2O$ catalyst during the OER activity. In addition, the stability of OER catalysts plays a vital role for exercising low cost and efficient catalysts for water splitting from the commercial point of view. As shown in Fig. 5d, the change in the OER polarization curve was insignificant after continuous 3000 LSV cycles of the $Cu_2(OH)PO_4/Co_3(PO_4)_2\cdot 8H_2O$ composite at the scan rate of 10 mV s^{-1}. LSV cycle stability suggested that the composite catalyst acted as a promising electrocatalyst, and the change in the overpotential at a current density of 10 mA cm^{-2} was found to be only 3 mV (from 234 mV to 237 mV) during the OER activity in an alkaline medium. We have also performed the chronoamperometry method for the stability test, and it was performed at an overpotential of 234 mV for 24 h, and the loss of current density after 24 h was almost negligible (Fig. 5e). We also studied chronopotentiometric measurements of the composite in 1.0 M KOH as a function of the current density (10 to 60 mA cm^{-2}), and in each stage, constant potential was obtained at different applied currents (Fig. 5f). $Cu_2(OH)PO_4/Co_3(PO_4)_2\cdot 8H_2O$ displayed overpotentials of 234, 265, 288, 306, 323 and 338 mV at a current densities of 10, 20, 30, 40, 50 and 60 mA cm^{-2}, respectively. We have also evaluated the electrochemically active surface area (ECSA) of the catalysts and the highest ECSA was obtained by $Cu_2(OH)PO_4/Co_3(PO_4)_2\cdot 8H_2O$ (117.5 cm^2), was higher than the that of $Co_3(PO_4)_2\cdot 8H_2O$ (43.2 cm^2) and $Cu_2(OH)PO_4$ (32.1 cm^2) (Fig. S1 and Table S3†). Interestingly, ECSA of $Cu_2(OH)PO_4/Co_3(PO_4)_2\cdot 8H_2O$ with a binder was calculated to be 96.8 cm^2, indicating that the external binder masked the active surface area of the catalyst during the OER process (Fig. S1†).

To investigate the bifunctional behaviour of the as-synthesised catalysts, we have studied the HER activity, and also determined the overpotential by LSV and the kinetics by the Tafel slope. LSV were obtained at a scan rate of 10 mV s^{-1} in 0.5 M H_2SO_4 (Fig. 6). It was observed that the $Cu_2(OH)PO_4/Co_3(PO_4)_2\cdot 8H_2O$ composite acquired a relatively low over potential of 138 mV in comparison of $Co_3(PO_4)_2\cdot 8H_2O$ (256 mV) and $Cu_2(OH)PO_4$ (459 mV) and Pt/C (32 mV), respectively. However, the $Cu_2(OH)PO_4/Co_3(PO_4)_2\cdot 8H_2O$ composites with the external binder showed a higher overpotential of 178 mV than the DNA-guided synthesised $Cu_2(OH)PO_4/Co_3(PO_4)_2\cdot 8H_2O$ composite for HER activity (Fig. 6a). To examine the sluggish kinetics of the catalysts, Tafel slopes were obtained from LSV and compared with that of Pt/C, which showed the lowest Tafel slope value of 41 mV dec^{-1}, whereas Tafel slopes for $Cu_2(OH)PO_4/Co_3(PO_4)_2\cdot 8H_2O$, $Cu_2(OH)PO_4/Co_3(PO_4)_2\cdot 8H_2O$ composites with an external binder, $Co_3(PO_4)_2\cdot 8H_2O$, $Cu_2(OH)PO_4$ were found to be 74 mV dec^{-1} 89 mV dec^{-1}, 106 mV dec^{-1} and 158 mV dec^{-1}, respectively (Fig. 6b). A change in the HER polarization curve after continuous 3000 cycles was insignificant at the scan rate of 10 mV s^{-1}, and this observation suggested that a change in the overpotential at current density of 10 mA cm^{-2} was found to be only 4 mV (from 138 mV to 142 mV)
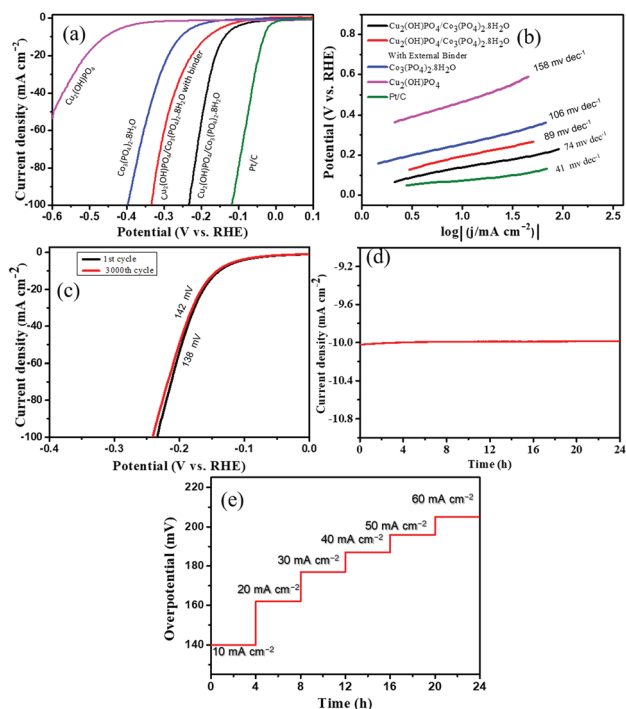
Fig. 6 (a) Linear sweep voltammograms plot and (b) the corresponding Tafel plots of $Cu_2(OH)PO_4/Co_3(PO_4)_2\cdot8H_2O$, $Cu_2(OH)PO_4/Co_3(PO_4)_2\cdot8H_2O$ with the external binder, $Co_3(PO_4)_2\cdot8H_2O$, $Cu(OH)PO_4$ and Pt/C, (c) polarization curves of the $Cu_2(OH)PO_4/Co_3(PO_4)_2\cdot8H_2O$ composite of 1st and 3000th cycles of continuous operation, (d) chronoamperometry study of the $Cu_2(OH)PO_4/Co_3(PO_4)_2\cdot8H_2O$ composite catalyst at an overpotential of 138 mV for 24 h. (e) Chronopotentiometric study of $Cu_2(OH)PO_4/Co_3(PO_4)_2\cdot8H_2O$ for HER in 0.5 M H_2SO_4 as a function of the current density.

(Fig. 6c). We have performed the chronoamperometry method at an overpotential of 138 mV for 24 h (Fig. 6d). Furthermore, we carried out chronopotentiometric measurements of the $Cu_2(OH)PO_4/Co_3(PO_4)_2\cdot8H_2O$ composite in 0.5 M H_2SO_4 as a function of the current density (10 to 60 mA cm^{-2}), and displayed overpotentials of 138, 162, 177, 187, 196 and 205 mV at current densities of 10, 20, 30, 40, 50 and 60 mA cm^{-2}, respectively (Fig. 6e and Table S3†). Different types of stability tests proved the long-term superior durability of the $Cu_2(OH)PO_4/Co_3(PO_4)_2\cdot8H_2O$ composite catalyst towards the HER activity in the acidic medium. All these electrochemical studies, namely LSV study, Tafel analysis and EIS investigation, revealed that $Cu_2(OH)PO_4/Co_3(PO_4)_2\cdot8H_2O$ exhibited a superior electrochemical HER activity over all other synthesised catalysts. The overpotential required to obtain a current density at 10 mA cm^{-2} in this study was compared with a transition metal phosphate nanostructure-based electrocatalyst reported in literature (Table S5†). The overpotentials (234 mV for OER and 138 mV for HER) shown by the electrocatalyst composed of the porous $Cu_2(OH)PO_4/Co_3(PO_4)_2\cdot8H_2O$ rolling pin shape were substantially comparable/higher than the previous reports. [1,3,9,11,27,29,31,32,47–54]

The overall potential of the DNA-based composite material in water splitting/electrocatalysis applications is due to the excellent adherence property of DNA, making it to stick comfortably over a variety of external substrates, such as carbon cloth, GC electrode and glass slide. The variety of functional groups of DNA and the green nature along with the ease of forming self-assemblies, DNA stands out to be an outstanding scaffold. This is beneficial for using metal-DNA scaffolds for interdisciplinary applications as the exposed active surface area would vary with respect to change in morphology. For both anode and cathode materials, electrode fabrication with external binders, such as Nafion, results in the swelling of catalytically active sites and hence poisons the activity. By using DNA materials, there is no need for the addition of external binders with metal-DNA colloidal solution. This is one of the best advantages of the DNA-based metal nanostructure synthesis and other systems as stable solutions for electrocatalytic studies. Also, in electrocatalytic studies, DNA exhibits utmost stability for long durations as discussed. At high overpotentials, the synergistic enhancement of OER activity is also affected from the phosphate backbones of DNA in addition to the catalytically active sites of the electrode surface. Without an external binder, this is an important advantage in DNA metallization, and the fast fabrication of electrodes makes them attractive over other methods of synthesis.

In order to investigate the morphological changes of the $Cu_2(OH)PO_4/Co_3(PO_4)_2\cdot8H_2O$ composite after the chronopotentiometric stability test, we have also performed XRD, FE-SEM and TEM analyses. XRD pattern (Fig. S5e†), SEM (Fig. S5a and b†) and TEM (Fig. S5c and d†) investigations clearly reveal that no structural deformation occurred after the catalytic execution. However, the surface crystallinity of the catalyst was lost to some extent in the edge of the nanostructure. Brunauer–Emmett–Teller (BET) study results with pore size distribution of the $Cu_2(OH)PO_4/Co_3(PO_4)_2\cdot8H_2O$ composite are displayed in Fig. S6,† and the pore diameter of the composite nanostructure was found to be 24.84 nm, which apprised that the material was porous in nature.

The results of the electrochemical studies combined with the superior properties, including the low overpotential, small Tafel slope, and large electrochemical active surface area, unequivocally proved the porous confinement on the $Cu_2(OH)PO_4/Co_3(PO_4)_2\cdot8H_2O$ surface. The porous confinement and rolling pin shape of the composite structure were the key factors to boost the OER and HER activity, making a competitive bifunctional catalyst that can potentially replace expensive noble metal catalysts. The excellent catalytic activity of the composite material could be attributed to the following factors: (i) the synergistic effect of different metals (ii) the pores on the surface of the material produced enough active sites required for the improved catalytic activity per geometric area (iii) the porous structure created a conducive environment for a close contact with the electrolyte, thus allowing more utilization of the active sites and (iv) the phosphate group affected the local Cu and Co geometry, facilitating the uptake of oxygen adsorbate leading to a favourable water adsorption and water oxidation and (v) the charge transfer resistance reduced upon the binding of genomic DNA with the catalyst.

Conclusion

We reported a novel approach to generate a porous $Cu_2(OH)PO_4/Co_3(PO_4)_2 \cdot 8H_2O$ rolling pin shape composite structure using a genomic DNA-mediated synthetic route to boost the electrocatalytic OER and HER. In addition, the incorporation of a biomolecule, for example, genomic DNA, provides to sustain OER without utilizing any binder molecules, like Nafion. Significantly, the porous $Cu_2(OH)PO_4/Co_3(PO_4)_2 \cdot 8H_2O$ rolling pin composite showed a superior OER performance with a small overpotential of 234 mV and the Tafel slope was 62 mV/dec at 10 mA cm^{-2}. Due to the synergistic effect and higher ESCA, the porous $Cu_2(OH)PO_4/Co_3(PO_4)_2 \cdot 8H_2O$ rolling pin shape composite disseminated faster kinetics towards both OER and HER activities with lower overpotentials. Thus, we believe that these sorts of new ways to deal with the integration of noble metals free on binary phosphate surfaces will open a new direction for the large hydrogen gas generation.

Conflicts of interest

There are no conflicts to declare.

Acknowledgements

References

1 M. A. Z. G. Sial, H. Lin and X. Wang, *Nanoscale*, 2018, **10**, 12975–12980.

2 A. Anwar, L. Chi Fung, A. Anwar, P. Jagadish, A. Numan, M. Khalid, S. Shahabuddin, R. Siddiqui and N. A. Khan, *Pathogens*, 2019, **8**, 260.

3 X. Bu, C. Chiang, R. Wei, Z. Li, Y. Meng, C. Peng, Y. Lin, Y. Li, Y. Lin and K. S. Chan, *ACS Appl. Mater. Interfaces*, 2019, **11**, 38633–38640.

4 J. Ma, Y. Kong, S. Liu, Y. Li, J. Jiang, Q. Zhou, Y. Huang and S. Han, *ACS Appl. Energy Mater.*, 2020, **3**, 11900–11906.

5 R. Biswas, P. Thakur, G. Kaur, S. Som, M. Saha, V. Jhajhria, H. Singh, I. Ahmed, B. Banerjee, D. Chopra, T. Sen and K. K. Haldar, *Inorg. Chem.*, 2021, **60**, 12355–12366.

6 D. Cheng, Z. Wang, C. Chen and K. Zhou, *Chem. Mater.*, 2019, **31**, 8026–8034.

7 R. Biswas, B. Banerjee, M. Saha, I. Ahmed, S. Mete, R. A. Patil, Y.-R. Ma and K. K. Haldar, *J. Phys. Chem. C*, 2021, **125**, 6619–6631.

8 R. Biswas, S. Singh, I. Ahmed, R. A. Patil, Y. R. Ma and K. K. Haldar, *ChemNanoMat*, 2021, **7**, 158–164.

9 H. Li, X. Kong, X. Geng, C. Gu, Z. Liu and J. Wang, *Electrochim. Acta*, 2021, **367**, 137562.

10 L. Gao, J. Xie, X. Ma, M. Li and L. Yu, *Nanoscale Res. Lett.*, 2017, **12**, 1–8.

11 S. S. Sankar, A. Rathishkumar, K. Geetha and S. Kundu, *Energy Fuels*, 2020, **34**, 12891–12899.

12 J. Xing, H. Li, M. M.-C. Cheng, S. M. Geyer and K. S. Ng, *J. Mater. Chem. A*, 2016, **4**, 13866–13873.

13 D. T. Tran, H. T. Le, N. H. Kim and J. H. Lee, *Appl. Catal., B*, 2019, **253**, 235–245.

14 J. Qi, W. Zhang and R. Cao, *ChemCatChem*, 2018, **10**, 1206–1220.

15 G. Aguilar-Armenta, M. Patino-Iglesias, J. Jiménez-Jiménez, E. Rodríguez-Castellón and A. Jiménez-López, *Langmuir*, 2006, **22**, 1260–1267.

16 M. Pramanik, R. R. Salunkhe, M. Imura and Y. Yamauchi, *ACS Appl. Mater. Interfaces*, 2016, **8**, 9790–9797.

17 P. Suganya, A. Venkadesh, J. Mathiyarasu and S. Radhakrishnan, *J. Solid State Electrochem.*, 2019, **23**, 3429–3435.

18 S. Wei, J. Yao and B. Shi, *Solid State Ionics*, 2017, **305**, 36–42.

19 D. Zhu, Q. Zhen, J. Xin, H. Ma, L. Tan, H. Pang and X. Wang, *Sens. Actuators, B*, 2020, **321**, 128541.

20 J. L. Zhang, S. Zhao, S. Sun, X. Lian, A. Tadich, D.-C. Qi, C. Gu, Z. Ma, Z. Li and W. Chen, *Chem. Mater.*, 2020, **32**, 8561–8566.

21 M. Tiemann, *Chem.–Eur. J.*, 2007, **13**, 8376–8388.

22 A. D. Trofimov, A. A. Ivanova, M. V. Zyuzin and A. S. Timin, *Pharmaceutics*, 2018, **10**, 167.

23 R. Sun, M. Åhlén, C.-W. Tai, É. G. Bajnóczi, F. de Kleijne, N. Ferraz, I. Persson, M. Strømme and O. Cheung, *Nanomaterials*, 2020, **10**, 20.

24 M. Parent, H. Baradari, E. Champion, C. Damia and M. Viana-Trecant, *J. Controlled Release*, 2017, **252**, 1–17.

25 Z. Wang, M. Liu, J. Du, Y. Lin, S. Wei, X. Lu and J. Zhang, *Electrochim. Acta*, 2018, **264**, 244–250.

26 B. Mahmoud, A. Mirghni, K. Oyedotun, D. Momodu, O. Fasakin and N. Manyala, *J. Alloys Compd.*, 2020, **818**, 153332.

27 W. Bian, Y. Huang, X. Xu, M. A. Ud Din, G. Xie and X. Wang, *ACS Appl. Mater. Interfaces*, 2018, **10**, 9407–9414.

28 Y. Zhan, M. Lu, S. Yang, C. Xu, Z. Liu and J. Y. Lee, *ChemCatChem*, 2016, **8**, 372–379.

29 A. Karmakar, K. Karthick, S. S. Sankar, S. Kumaravel, M. Ragunath and S. Kundu, *Inorg. Chem.*, 2021, **60**, 2680–2693.

30 W. J. Moon and J. Liu, *Adv. Mater. Interfaces*, 2020, 7, 2001017.

31 S. Anantharaj, P. E. Karthik, B. Subramanian and S. Kundu, *ACS Catal.*, 2016, **6**, 4660–4672.

32 K. Karthick, S. N. Jagadeesan, P. Kumar, S. Patchaiammal and S. Kundu, *Inorg. Chem.*, 2019, **58**, 6877–6884.

33 S. Kumaravel, M. P. Kumar, P. Thiruvengetam, N. Bandla, S. S. Sankar, S. Ravichandran and S. Kundu, *Inorg. Chem.*, 2020, **59**, 14501–14512.

34 Y. Zhu, J. Ren, X. Zhang and D. Yang, *Nanoscale*, 2020, **12**, 13297–13310.

35 S. Kumaravel, M. Subramanian, K. Karthick, A. Sakthivel, S. Kundu and S. Alwarappan, *ACS omega*, 2021, **6**, 19162–19169.

36 K. Karthick, S. Anantharaj, S. R. Ede, S. S. Sankar, S. Kumaravel, A. Karmakar and S. Kundu, *Adv. Colloid Interface Sci.*, 2020, 102205.

37 S. Tanwar, V. Kaur, G. Kaur and T. Sen, *J. Phys. Chem. Lett.*, 2021, **12**, 8141–8150.

38 L. H. Tan, H. Xing and Y. Lu, *Acc. Chem. Res.*, 2014, **47**, 1881–1890.

39 J. Doyle, in *Molecular techniques in taxonomy*, Springer, 1991, pp. 283–293.

40 Y.-J. Cheng, W.-W. Guo, H.-L. Yi, X.-M. Pang and X. Deng, *Plant Mol. Biol. Rep.*, 2003, **21**, 177–178.

41 A. Samal, D. P. Das and G. Madras, *Sci. Rep.*, 2018, **8**, 1–18.

42 C.-Z. Yuan, Y.-F. Jiang, Z. Wang, X. Xie, Z.-K. Yang, A. B. Yousaf and A.-W. Xu, *J. Mater. Chem. A*, 2016, **4**, 8155–8160.

43 H. Shao, N. Padmanathan, D. McNulty, C. O' Dwyer and K. M. Razeeb, *ACS Appl. Mater. Interfaces*, 2016, **8**, 28592–28598.

44 I. Ahmed, R. Biswas, R. A. Patil, K. K. Halder, H. Singh, B. Banerjee, B. Kumar, Y.-R. Ma and K. K. Haldar, *ACS Appl. Nano Mater.*, 2021, **4**, 12672–12681.

45 M. Zhang, Z. Luo, M. Zhou, G. Zhang, K. A. Alamry, L. A. Taib, A. M. Asiri and X. Wang, *Appl. Catal., B*, 2017, **210**, 454–461.

46 Q. Wang, X. Ma, P. Wu, B. Li, L. Zhang and J. Shi, *Nano Energy*, 2021, **89**, 106326.

47 S. Zhao, C. Li, H. Huang, Y. Liu and Z. Kang, *J. Materiomics.*, 2015, **1**, 236–244.

48 X. Li, Q. Zha and Y. Ni, *ACS Sustainable Chem. Eng.*, 2019, **7**, 18332–18340.

49 P. W. Menezes, C. Panda, C. Walter, M. Schwarze and M. Driess, *Adv. Funct. Mater.*, 2019, **29**, 1808632.

50 M. Ge, X. Zhang, S. Xia, W. Luo, Y. Jin, Q. Chen, H. Nie and Z. Yang, *Chin. J. Chem.*, 2021, **39**, 2113–2118.

51 T. S. Kim, H. J. Song, M. A. Dar, H. W. Shim and D. W. Kim, *J. Am. Ceram. Soc.*, 2018, **101**, 3749–3754.

52 L. T. Le, T. T. Nguyen, T. T. Nguyen, M. T. Nguyen, T. T. Ung and P. D. Tran, *Chem.–Asian J.*, 2020, **15**, 1873–1880.

53 K. S. Bhat and H. Nagaraja, *J. Sci.: Adv. Mater. Devices*, 2020, **5**, 361–367.

54 M. Zheng, Q. Chen and Q. Zhong, *Dalton Trans.*, 2021, **50**, 13320–13328.